High Control Authority Three-Dimensional Aircraft Control Surfaces Using Coflow Jet

Kewei Xu* and Gecheng Zha†
University of Miami, Coral Gables, Florida 33124

https://doi.org/10.2514/1.C035727

This paper conducts improved delayed detached eddy simulation (IDDES) to numerically investigate the performance of a three-dimensional (3D) aircraft control surface using coflow jet (CFJ) active flow control. For the numerical validation with the baseline control surface that has a large flow separation, the predicted lift coefficient C_L and drag coefficient C_D achieve a very good agreement with the experiment, and the maximum discrepancy is less than 3.8%. For the 3D CFJ control surface, a small momentum coefficient C_μ of 0.025 generates a 28% of C_L increase at 0° sideslip angle with the flow separation removed. At the same time, a higher corrected aerodynamic efficiency $(C_L/C_D)_c$ than the baseline is obtained. With C_μ of 0.26, the CFJ control surface has its C_L increased by 99.25% and the C_D dropped by 52%. A phenomenon not observed in a regular CFJ wing without flap is that the second suction peak at the flap shoulder is higher than the leading-edge suction peak due to the attached flow with a sharp turning. The CFJ control surface can also sustain a substantially higher stall sideslip angle and flap deflection angle. In conclusion, the 3D control surface using CFJ active flow control is demonstrated by numerical simulation that it can substantially increase the control authority at low energy expenditure.

Nomenclature

C	=	chord length
C_D	=	drag coefficient
C_L	=	lift coefficient
C_L/C_D	=	aerodynamic efficiency
$(C_L/C_D)_c$	=	aerodynamic efficiency corrected for coflow jet airfoil
C_p	=	pressure coefficient, $(P - P_\infty)/([1/2]\rho_\infty V_{\infty t}^2)$
C_μ	=	jet momentum coefficient, $\dot{m}_j V_j/([1/2]\rho_\infty V_\infty^2 S)$
c_p	=	constant pressure specific heat
D	=	total drag on the airfoil
H_t	=	total enthalpy
L	=	total lift on the airfoil
M	=	Mach number
M_j	=	injection Mach number
$\dot{m}$	=	mass flow rate
$\overline{\dot{m}}$	=	nondimensional mass flow rate, $\dot{m}/(V_\infty \rho_\infty S)$
P	=	coflow jet pumping power
P_c	=	power coefficient, $P/([1/2]\rho_\infty V_\infty^3 S)$
P_t	=	total pressure
P_∞	=	static pressure of freestream
R_e	=	Reynolds number
S	=	planform area of the wing
T_t	=	total temperature
V_j	=	injection velocity
V_∞	=	freestream velocity
$V_{\infty t}$	=	freestream velocity normal to the wing leading edge, used to calculate C_p
α	=	angle of attack
β	=	sideslip angle
Γ	=	total pressure ratio of coflow jet pump
γ	=	air specific heats ratio
δ	=	deflection angle
η	=	coflow jet pumping system efficiency
θ_1	=	angle between the injection slot surface and a line normal to the airfoil chord
θ_2	=	angle between the suction slot surface and a line normal to the airfoil chord
ρ_∞	=	freestream density

Subscripts

c	=	corrected
j	=	jet

I. Introduction

AIRCRAFT control surfaces such as vertical tails, horizontal tails, and canards are responsible for maintaining the aircraft stability. Control surfaces need to have high control authority by generating sufficient lift with rapid response time to keep the aircraft trimmed. To achieve such performance, control surfaces usually have large sizes, which bring severe penalty of weight, drag, and energy consumption.

Active flow control (AFC) as a means to enhance lift has great potential to reduce the size and weight of control surfaces [1–7]. AFC is used to control the separated flow of vertical tails to enhance aerodynamic performance and mitigate flutter [8–17]. The research of Boeing and NASA [8–15] on vertical tails using sweeping jets and synthetic jets AFC represents the state-of-the-art. Rathay et al. [8] conducted wind tunnel experiments on a swept and tapered tail with a 29.6% chord rudder. Using flow control, the side force was increased by up to 18% at moderate rudder deflections with the AFC actuators operating at dimensionless frequency of O(10) [8] and a momentum coefficient $C_\mu = 0.00721$. Compared with synthetic jets, sweeping jets have higher C_μ output and corresponding jet velocity. Thus sweeping jets were selected over the synthetic jets by Boeing/NASA team for the subsequent full-scale AFC wind tunnel tests [9,10].

The vertical tails with sweeping jets AFC were successfully tested on subscale models [11,12], full-scale models [9,10], and finally in flight [9]. The subscale test was performed at a 14% scaled model of Caltech, and more than 50% of the side force enhancement was achieved by sweeping jet actuation with the momentum coefficient C_μ of 0.017. The full-scale vertical tail model equipped with sweeping jets AFC was tested at a nominal speed of 100 knots ($M_\infty \sim 0.15$, $Re \sim 15$ million), a maximum speed of 130 knots ($M_\infty \sim 0.2$, $Re \sim 20$ million), and across the vertical tail flight envelop for rudder deflections (0° to 30°) and sideslip angles (0° to −7.5°). A 31-actuator

Presented as Paper 2019-3168 at the AIAA Aviation 2019 Forum, Dallas, TX, June 17–21, 2019; received 19 September 2019; revision received 8 June 2020; accepted for publication 11 June 2020; published online 14 July 2020.

*Ph.D. Candidate, Department of Mechanical and Aerospace Engineering.
†Professor, Department of Mechanical and Aerospace Engineering; gzha@miami.edu. Associate Fellow AIAA.

sweeping jets configuration produces significant flow attachment on the rudder, which results in 20% increase in side force for the maximum rudder deflection of 30° at the sideslip angle of 0° and −7.5°. Subsequently, the sweeping-jet-enhanced vertical tail was flown on the Boeing 757 ecoDemonstrator in the spring of 2015. A side force increase of 13–16% was estimated at a 30° rudder deflection for the critical sideslip angle range between 0° and −7.5° with the sweeping jets. Kara [16,17] analyzed the complex flow inside the sweeping jets for design optimization of actuator geometry with minimum pressure loss. However, the sweeping jets tend to suffer large energy loss due to the jet sweeping, 360° turning, and massive flow separation. Furthermore, the system will also suffer an energy penalty due to introducing the air flow from engine bleed. The other challenging issue using engine bleed for flow control is that when the engines are idle at landing, they may not be able to provide sufficient mass flow.

Recently, Zhang et al. [18] conducted two-dimensional (2D) numerical simulation to study a new aircraft control surfaces using coflow jet (CFJ) airfoil [2,5,19–27], which is a zero-net-mass-flux (ZNMF) flow control that does not need to use engine bleed. The CFJ control surface is proven to be very effective with low energy expenditure. It can substantially reduce the control surface size and weight and simplify the control surface system. Xu et al. [28] studied the energy expenditure of CFJ control surfaces. The parametric study of injection slot size and slot location is conducted to acquire the optimum aerodynamic efficiency of CFJ actuators. Besides, two methods are studied to minimize the CFJ control surface drag when it is not in use at cruise condition. One method is to use a very light jet at cruise and the other is to cover the slots using a small moving surface segment [28]. Previous CFJ control surface studies [18,28] are mainly focused on 2D, which do not reflect the complexity of three-dimensional (3D) control surface with sweep, low aspect ratio, and tapper.

The objective of this paper is to numerically apply CFJ to a realistic 3D vertical control surface to demonstrate its superior performance. The 3D swept vertical tail tested by Seele et al. [12] is used as the baseline for comparison. The effects of CFJ momentum coefficient C_μ, deflection angle δ, and sideslip angle β are investigated. This paper is based on the preliminary simulation of the 3D CFJ vertical tail study conducted by Xu and Zha [29] with more refined validation, results, and analysis.

In the CFJ wing, an injection slot near leading edge (LE) and a suction slot near trailing edge (TE) on the wing suction surface are created as shown in Fig. 1. A small amount of mass flow is drawn into the wing near the TE, pressurized and energized by a microcompressor pumping system inside the wing, and injected near the LE tangential to the main flow. The whole process does not add any mass flow to the system and hence is a ZNMF flow control.

As described in [18,28], a symmetric CFJ airfoil is used for the control surface as shown in Fig. 2. The injection slot and the suction slot are distributed on both sides of the CFJ control surface airfoil. When one side CFJ is working to generate side force, the other side CFJ is closed. The 3D CFJ control surface is created by extruding and tapering the 2D CFJ airfoil in spanwise direction.

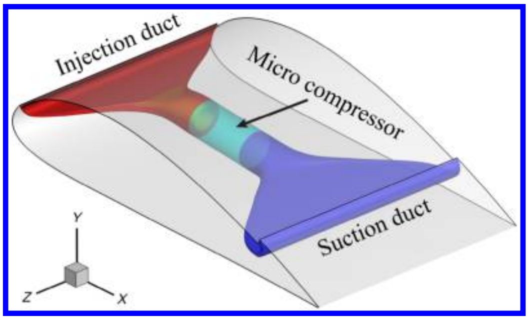

Fig. 1 Schematics of the CFJ wing.

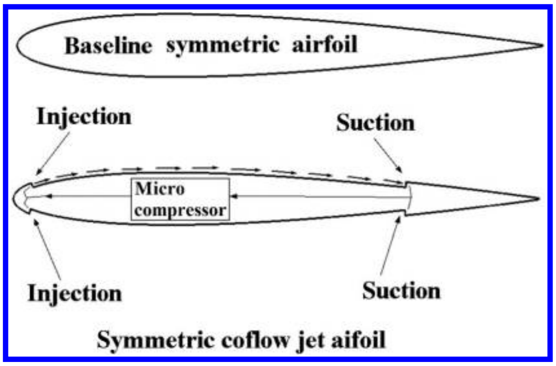

Fig. 2 Schematics of the baseline and the CFJ control surface airfoils.

II. CJF Parameters

This section lists the important parameters used to evaluate aerodynamic performance of a CFJ airfoil.

A. Jet Momentum Coefficient

The jet momentum coefficient C_μ is a parameter used to quantify the jet intensity. It is defined as

$$C_\mu = \frac{\dot{m} V_j}{(1/2)\rho_\infty V_\infty^2 S} \tag{1}$$

where $\dot{m}$ is the injection mass flow, V_j is the mass-averaged injection velocity, ρ_∞ and V_∞ denote the freestream density and velocity, and S is the planform area.

B. Lift and Drag Calculation

For computational fluid dynamics (CFD) simulation, the full reactionary forces produced by the momentum and pressure at the injection and suction slots are included by using control volume analysis. Zha et al. [19] give the following formulations to calculate the lift and drag due to the jet reactionary force for a CFJ airfoil. By considering the effects of injection and suction jets on the CFJ airfoil, the expressions for these reactionary forces are given as

$$F_{x_{cfj}} = (\dot{m}_j V_{j1} + p_{j1} A_{j1}) * \cos(\theta_1 - \alpha) \\ -(\dot{m}_j V_{j2} + p_{j2} A_{j2}) * \cos(\theta_2 + \alpha) \tag{2}$$

$$F_{y_{cfj}} = (\dot{m}_{j1} V_{j1} + p_{j1} A_{j1}) * \sin(\theta_1 - \alpha) \\ + (\dot{m}_{j2} V_{j2} + p_{j2} A_{j2}) * \sin(\theta_2 + \alpha) \tag{3}$$

where the subscripts 1 and 2 stand for the injection and suction, respectively, and θ_1 and θ_2 are the angles between the injection and suction slot's surface and a line normal to the airfoil chord. α is the angle of attack (AoA).

The total lift and drag on the airfoil can then be expressed as

$$D = R_x' - F_{x_{cfj}} \tag{4}$$

$$L = R_y' - F_{y_{cfj}} \tag{5}$$

where R_x' and R_y' are the surface integral of pressure and shear stress in x (drag) and y (lift) directions excluding the internal ducts of injection and suction. For CFJ wing simulations, the total lift and drag are calculated by integrating Eqs. (4) and (5) in the spanwise direction.

C. Power Coefficient

The power consumption is determined by the jet mass flow and total enthalpy change as follows:

$$P = \dot{m}(H_{t1} - H_{t2}) \tag{6}$$

where H_{t1} and H_{t2} are the mass-averaged total enthalpy in the injection cavity and suction cavity, respectively; P is the power required by the pump, and $\dot{m}$ is the jet mass flow rate. Introducing P_{t1} and P_{t2} as the mass-averaged total pressure in the injection and suction cavity, respectively, the pump efficiency η, and the total pressure ratio of the pump $\Gamma = (P_{t1}/P_{t2})$, the power consumption is expressed as

$$P = \frac{\dot{m} c_p T_{t2}}{\eta} \left(\Gamma^{(\gamma-1)/\gamma} - 1 \right) \tag{7}$$

where γ is the specific heat ratio equal to 1.4 for air, and η is the microcompressor efficiency with a typical value of 80% [27,30], but in this paper it is assumed as 100% to provide the required CFJ power. Equation (7) indicates that the power required for CFJ is linearly determined by the mass flow rate and exponentially by the total pressure ratio. This relationship in fact applies to all the AFCs based on fluidic actuation. Thus, C_μ is not a suitable parameter to represent the power consumption of AFC [5,31,32]. For example, a high C_μ could have a substantially lower power consumption than a lower C_μ if the large C_μ is created by a high mass flow rate and low jet velocity, which only needs a low total pressure ratio [5,31,32]. Because CFJ flow control is ZNMF, all the mass flow is generated locally and a high mass flow or high C_μ is not a limitation for CFJ application. This is very different from the circulation control (CC) airfoil, for which the mass flow needs to be introduced from external source (e.g., engine bleed).

The power coefficient is expressed as

$$P_c = \frac{P}{(1/2)\rho_\infty V_\infty^3 S} \tag{8}$$

D. Corrected Aerodynamic Efficiency

The conventional wing aerodynamic efficiency is defined as

$$\frac{C_L}{C_D} \tag{9}$$

For the CFJ wing, the ratio above still represents the pure aerodynamic relationship between lift and drag. However, because CFJ AFC consumes energy, the ratio above is modified to take into account the energy consumption of the pump. The formulation of the corrected aerodynamic efficiency for CFJ wings is

$$\left(\frac{L}{D}\right)_c = \frac{C_L}{C_D + P_c} \tag{10}$$

where P_c is the power coefficient, and L and D are the lift and drag generated by the CFJ wing. The formulation above converts the power consumed by the CFJ into a force P/V_∞, which is added to the aerodynamic drag D. If the pumping power is set to 0, this formulation returns to the aerodynamic efficiency of a conventional wing.

III. Numerical Algorithm

The in-house high-order-accuracy CFD code Flow-Acoustics-Structure Interaction Package (FASIP) is used to conduct the numerical simulation. The 3D improved delayed detached eddy simulation (IDDES) [33–36] turbulence model is used. A third-order Weighted Essentially Non-Oscillatory (WENO) scheme for the inviscid flux [37–39] and a second-order central differencing for the viscous terms are employed to discretize the Navier–Stokes equations. The low diffusion Roe scheme used as the approximate Riemann solver is used with the WENO scheme to evaluate the inviscid fluxes. Implicit time marching method using Gauss–Seidel line relaxation is used to achieve a fast convergence rate [40]. Parallel computing is implemented to save wall clock simulation time [41]. The FASIP code is intensively validated for various steady and unsteady 2D and 3D flows, including full aircraft [24,42,43], multistage compressors [44–48], aeroelasticity flows [49–54], and for CFJ 2D and 3D airfoil simulations [5,19–21,24–26,36,55–57]. Because the experimental results reported are time-averaged steady-state results, the numerical results are also presented as the time-averaged results after the flow and all the aerodynamic forces become statistically stable.

IV. Baseline Control Surface Validation

The 3D vertical tail with no flow control tested and simulated in [9–12,58] is used as the baseline in this study for comparison. The baseline vertical tail is tapered, swept with 42°, and stacked using NACA0012 airfoil. It has a 35% chord of flap length, a span of 1.067 m, a mean aerodynamic chord (MAC) of 0.538 m, and a flap deflection angle of 30°. In the tested control surface model, there is a very small gap between the front main control surface and the flap when the flap is deflected. This small gap is considered as insignificant to affect the 3D control surface aerodynamic performance and is thus not simulated for simplicity.

The freestream conditions used in the present study are the same conditions as given by Seele et al. in the experiment [12], which has the Reynolds number $Re_\infty = 1.36 \times 10^6$, incoming flow velocity $V_\infty = 40$ m/s (about Mach 0.12), and sideslip angle $\beta = 0°$.

The mesh topology is shown in Fig. 3. The computational domain is meshed using O-type grid with the mesh size of 6.14 million cells ($480 \times 80 \times 160$). Mesh refinement study is also conducted by doubling the number of cells in i, j, and k directions, respectively,

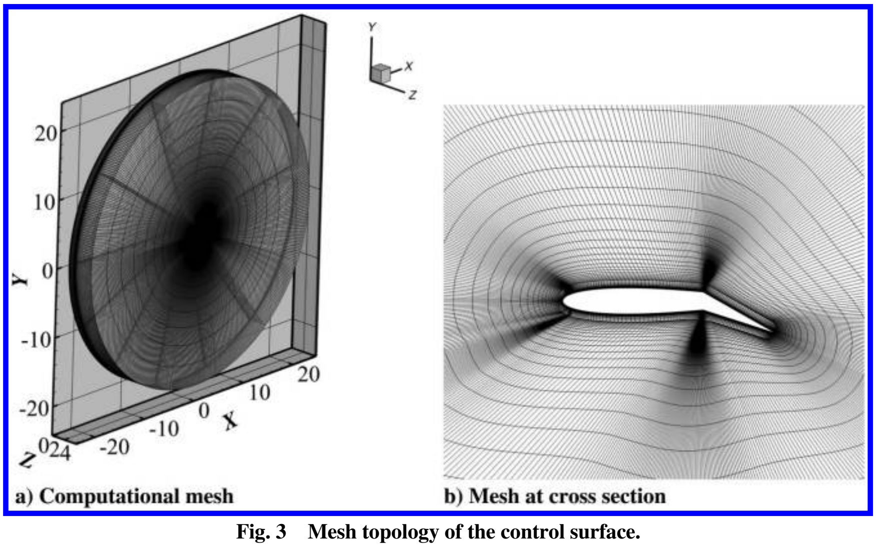

Fig. 3 Mesh topology of the control surface.

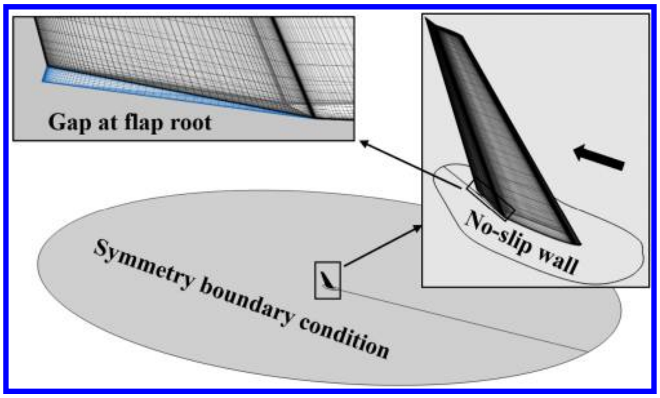

Fig. 4 Boundary conditions and mesh details at wing root.

as $960 \times 80 \times 160$, $480 \times 160 \times 160$, and $480 \times 80 \times 320$. The zero gradient condition is applied at far field in the span direction away from the tip. Radial far-field boundary is located at 30 times chord length, where the total pressure, total temperature, and flow angle are specified at the far-field inlet and the static pressure is specified at the outlet to match the freestream Mach number. The boundary conditions set up at wing root plane are illustrated in Fig. 4. A no-slip wall condition is imposed on the domain around the wing root to simulate the wind tunnel testing condition, whereas the outer root domain uses the symmetry boundary condition. This setup is similar to the boundary condition used by Vatsa et al. [58]. For all other solid wall surfaces, the no-slip wall boundary condition is enforced.

Table 1 shows the C_L and C_D comparison between the experiment and the CFD simulations with mesh refinement study. A good agreement is achieved using the baseline mesh with C_L deviation of 3.8% and C_D deviation of 3.6% considering the massively separated flow due to the 30° deflected flap. As the reference, the CFD results predicted by Vatsa et al. [58] using $k-\epsilon$ turbulence model with lattice Boltzmann model (LBM) flow solver are also presented Table 1. The C_L and C_D predicted by Vatsa et al. [58] have a 9.5 and 8.9% deviation from the experiment, respectively, larger than the 3.8 and 3.6% of the present prediction. This indicates that it is challenging to predict the control surface flow accurately when there is a massive flow separation. It also indicates that the present IDDES results are validated with high accuracy.

Table 2 presents the standard deviation (SD) of the mesh refinement results and their uncertainty, where Err C_L and Err C_D stand for the results variation between the refined meshes and the baseline mesh. It shows that the lift coefficient C_L has a maximum uncertainty of 2.1%, and the drag coefficient C_D has a maximum uncertainty of 2.8%. These results are within acceptable accuracy for this highly separated flow, which indicates that the baseline mesh is reasonably converged.

Figure 5 shows the time histories of the lift and drag coefficients. The results are stable after the characteristic time of 20. The SDs of the lift and drag coefficients for the last 200 time steps are in the order of 10^{-9} to 10^{-5} and are virtually machine zero compared with the C_L and C_D at order of 1.

The computed results are further validated by examining the wing surface pressure coefficient distributions (C_p). Three spanwise locations shown in Fig. 6 are selected for comparison: inboard (40% span of at LE), middle (70% span of at LE), and outboard (89% span of at LE). Figure 7 shows that the experimental and predicted pressure coefficients agree very well for all the spans. Results predicted by Vatsa et al. [58] are also plotted in Fig. 7 for comparison. The pressure coefficient predicted by the present IDDES agrees with the experiment very well from the LE to 65% chord because there is no flap and no flow separation in that part. The deviation is more at the flap, which has a flow separation at a deflection angle of 30°. For the inboard and outboard locations, the root vortex and tip vortex also affect the numerical results. The simulation of Vatsa et al. [58] overpredicts the pressure on the pressure surface for all the span locations. They also overpredict the LE suction peak and underpredict the second suction peak at the flap deflection location. For the 40% span location at X/C of 75%, a sharp C_p spike is observed in the experiment caused by the streamwise vortex [12]. Both the present simulation and the simulation of Vatsa et al. [58] fail to predict this pressure spike due to the massive separated flow at the flap.

Table 1 Simulation results of the baseline control surface with mesh refinement studies

Case	Mesh size	β, deg	$Re \times 10^6$	C_L	C_D
Experiment [58]	——	0	1.36	0.78	0.112
Vatsa et al. [58]	——	0	1.36	0.854	0.102
Baseline mesh	$480 \times 80 \times 160$	0	1.36	0.750	0.108
Doubled in i direction	$960 \times 80 \times 160$	0	1.36	0.734	0.108
Doubled in j direction	$480 \times 160 \times 160$	0	1.36	0.753	0.105
Doubled in k direction	$480 \times 80 \times 320$	0	1.36	0.745	0.105

Table 2 Standard deviation and uncertainty of the converged C_L and C_D

Case	SD of C_L	Err C_L, %	SD of C_D	Err C_D, %
Baseline	1.75×10^{-7}	——	8.36×10^{-9}	——
Doubled in i direction	5.29×10^{-7}	2.1	1.76×10^{-7}	0.0
Doubled in j direction	1.11×10^{-6}	0.3	1.32×10^{-7}	2.8
Doubled in k direction	2.19×10^{-5}	0.7	9.66×10^{-6}	2.8

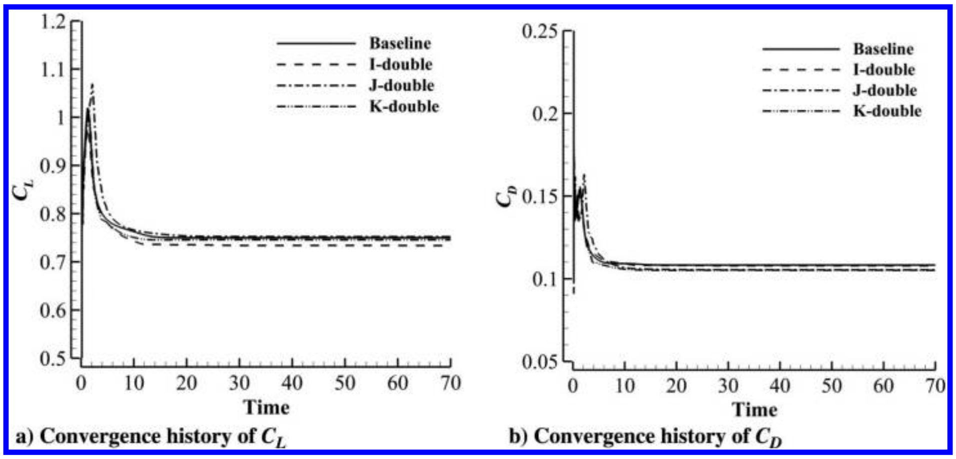

Fig. 5 Convergence history of simulations of the baseline control surface.

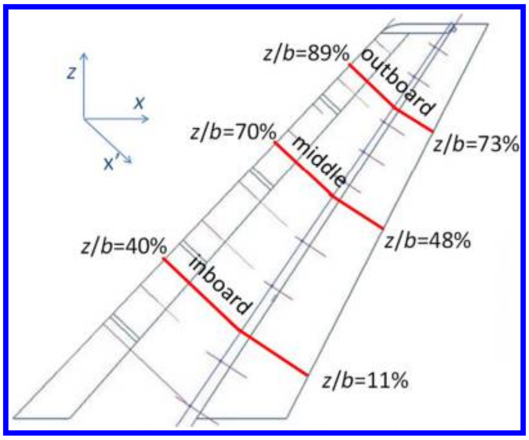

Fig. 6 Illustration of spanwise pressure tap rows (picture adopted from [58]).

Figures 8a–8c show the Mach contours of the baseline control surface at the three span locations corresponding to Fig. 6 at 40% span, 70% span, and 89% span. They display the flow separation at the 30° deflected flap. Figure 8d show the streamlines colored by Mach number on those span sections and the 3D flowfield. The massive flow separation on the flap forms a vortex tube rolling upward and connecting to the tip vortex.

V. 3D CFJ Control Surface

The 3D CFJ control surface shown in Fig. 9 is created based on the baseline wing by adding injection slots (red) near the LE and suction slots (blue) right upstream of flap deflection location. The basic CFJ control airfoil is the same as the one shown in the lower part of Fig. 2. Because only one side of CFJ is simulated, the injection and suction slots are created only on one side of the control surface. The CFJ slots on the other side are treated as steps to represent the closed slot conditions as the green part shown in Fig. 9. In the present study, the injection slot is located at $4\%C$ with a size of $0.9\%C$, and the suction slot is located at $63\%C$ with a size of $1\%C$.

Figure 10 is the cross section of 3D CFJ control surface. In our typical simulations, the simulated injection mass will flow through an internal channel as illustrated in yellow in Fig. 10. However, in this study, the injection duct is shortened to be near the injection slot as shown in red color in Fig. 10. The shortened duct is a numerical treatment to avoid the jet deflection. The control surface has a swept angle, which makes the CFJ injection duct also swept. Therefore, the turning section of the injection duct shown in yellow color in Fig. 10 will form a swept wall in spanwise direction. When jet flow hits this swept wall, it will be deflected as illustrates in the Fig. 11. Because of the deflection, the jet may not be aligned with freestream flow as desired. It is quite time consuming to adjust the flow incidence hitting the turning duct wall so that the deflection can be aligned with the main flow. The shortened duct adopted is placed immediately upstream of the injection slot to avoid the turning part of the duct. It is a numerical treatment to focus on the effect of the CFJ and leave the details of the jet deflection alignment as future work.

A. Jet Momentum Coefficient C_μ Variation

Five jet momentum coefficients of $C_\mu = 0.025, 0.05, 0.1, 0.2$, and 0.26 are studied with the sideslip angle β fixed at 0° and the flap deflection angle δ fixed at 30°. Table 3 compares the aerodynamic

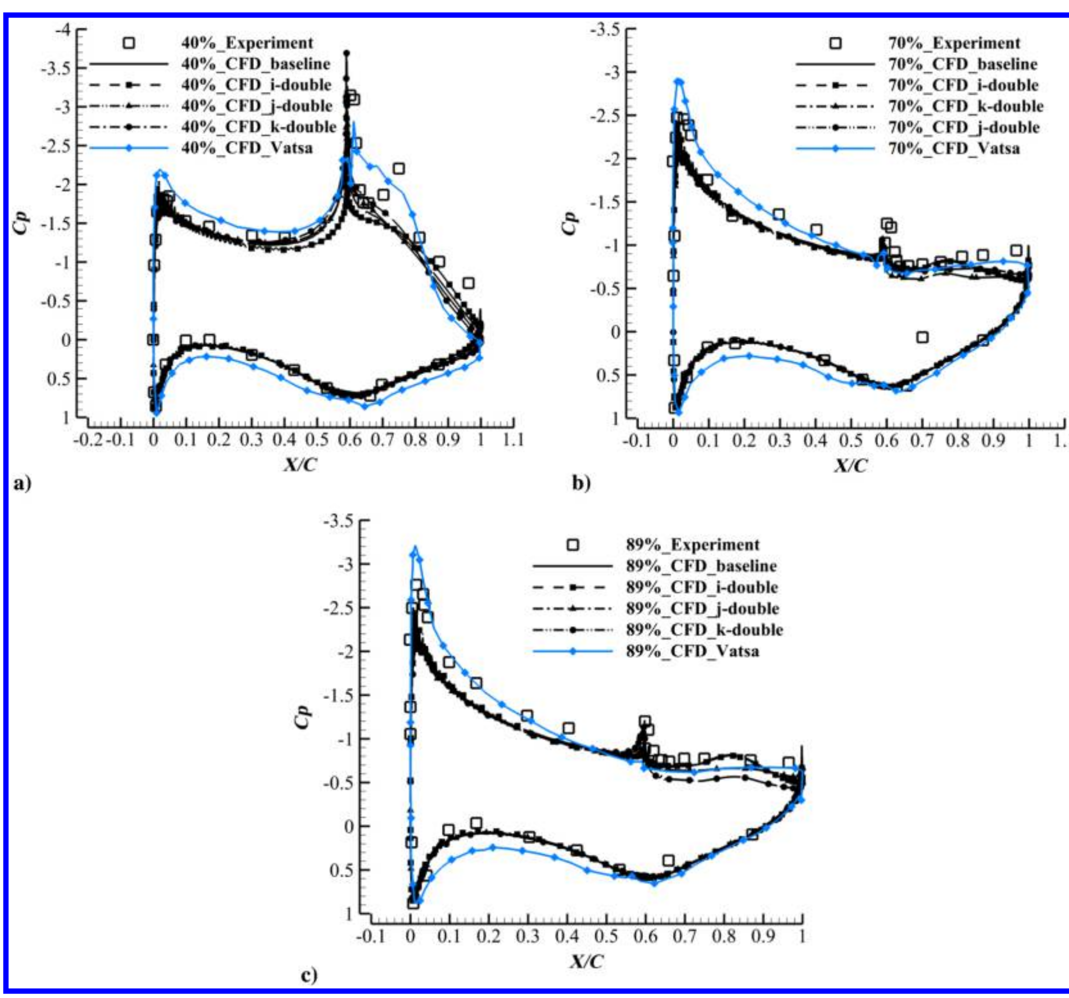

Fig. 7 Comparison of the predicted pressure coefficients with experiment and the results of Vatsa et al. [58] at a) inboard, b) middle span, and c) outboard.

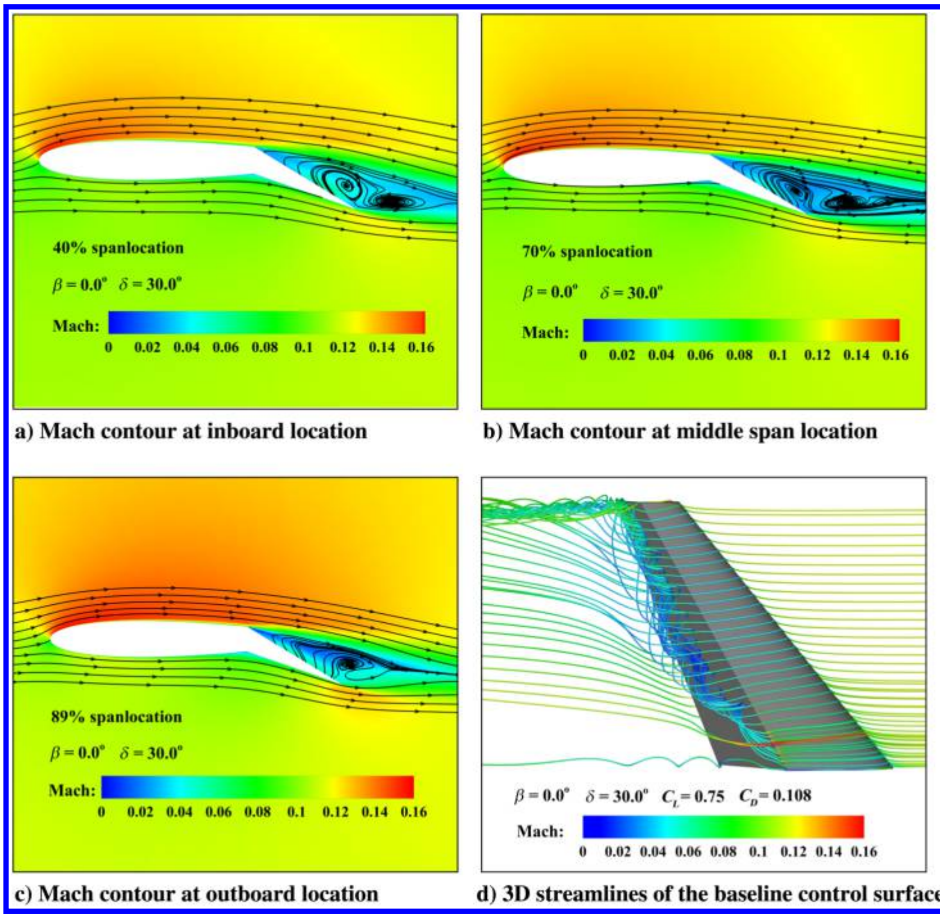

Fig. 8 Flowfield details of the baseline control surface.

parameters between the baseline and controlled control surfaces. Substantial C_L enhancement is achieved for all the CFJ control surfaces. The increase of C_μ augments the C_L, the power coefficient P_c, and the aerodynamic ratio of lift to drag (C_L/C_D). It significantly decreases the drag coefficient while increasing the lift coefficient due to the CFJ supersuction effect at the LE that reduces pressure drag. The overall corrected aerodynamic efficiency $(C_L/C_D)_c$ is decreased due to the more rapid increase of the CFJ power coefficient when the C_μ and lift coefficient are increased. As the C_μ is increased from 0.025 to 0.1, the drag coefficient is about the same. When the C_μ is increased to 0.26, the drag coefficient is sharply decreased due to the supersuction effect at the control surface LE. It is noted that at a low C_μ of 0.025, the C_L is increased by 28% compared with the baseline and $(C_L/C_D)_c$ is also slightly increased.

Increasing the lift coefficient of the control surface is the main approach to increase the control authority. The CFJ control surface with C_μ of 0.26 achieves a C_L of 1.494, about twice of the baseline control surface lift coefficient. This means that the CFJ control surface size can be reduced to half of the baseline one. At the same time,

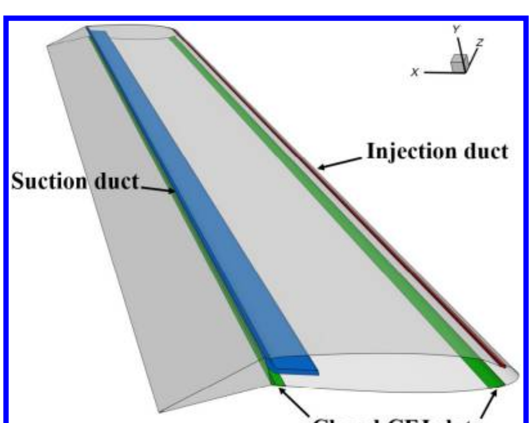

Fig. 9 Geometry of the 3D CFJ control surface.

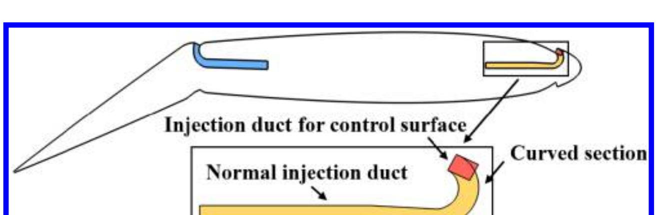

Fig. 10 Cross section of the 3D CFJ control surface.

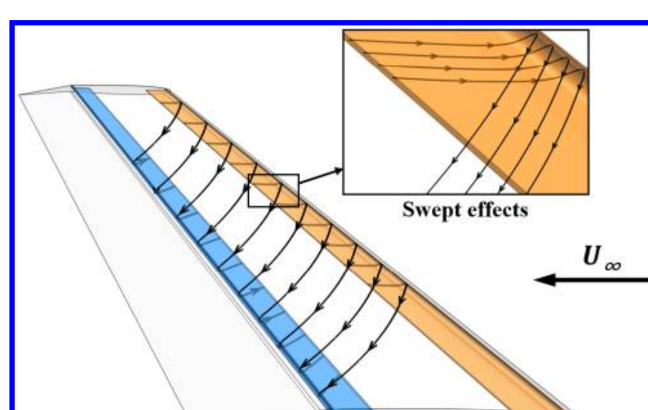

Fig. 11 Illustration of swept effects.

Table 3 Aerodynamic performance of the control surface with different C_μ

Case	C_L	ΔC_L, %	C_D	P_c	C_L/C_D	$(C_L/C_D)_c$	M_j	$\bar{\dot{m}}$	Γ
Baseline	0.75	——	0.108	——	6.93	6.93	——	——	——
Baseline EXP [58]	0.78	——	0.112	——	6.96	6.96	——	——	——
SWJ $C_\mu = 0.005$ EXP [58]	0.92	17.8	0.106	——	8.67	——	——	——	——
CFJ $C_\mu = 0.025$	0.96	28.1	0.109	0.026	8.84	7.09	0.12	0.011	1.02
CFJ $C_\mu = 0.05$	1.13	50.7	0.116	0.054	9.72	6.64	0.17	0.017	1.03
CFJ $C_\mu = 0.1$	1.30	73.3	0.110	0.198	11.9	4.23	0.26	0.024	1.08
CFJ $C_\mu = 0.2$	1.45	93.3	0.077	0.507	18.8	2.48	0.36	0.034	1.15
CFJ $C_\mu = 0.26$	1.49	99.3	0.05	0.768	28.8	1.82	0.40	0.039	1.20

C_L/C_D is increased to 28.8, more than 4 times higher than that of the baseline. However, corrected aerodynamic efficiency $(C_L/C_D)_c$ is decreased by 65%. In other words, the doubled lift and halved drag require more energy. For the injection jet Mach number normal to the swept slot, Table 3 shows its variation with C_μ. Note that the incoming freestream Mach number is 0.1. The injection jet Mach number normal to the slot varies from 0.12 at $C_\mu = 0.025$ to 0.4 at $C_\mu = 0.26$.

As explained in Eq. (7), a high C_μ such as 0.26 is not a limitation for CFJ flow control because it is a ZNMF flow control. Because a low C_μ of 0.025 is already very effective, the high C_μ of 0.26 studied here is an example to demonstrate how much extent that the control authority can be enhanced. It is not a necessary requirement. Because the control surface may be used for a very short transient time, the increased energy consumed by the control surface may hence be negligible compared with the size, drag, and weight reduction benefit brought to the aircraft for the whole mission.

The freestream Mach number of 0.1 studied in this paper is selected so that the simulation can be compared with the wind tunnel experiment. It is expected that the effectiveness of CFJ control surface is not restricted to such low Mach number. The previous studies indicate that CFJ is effective up to high subsonic and transonic Mach number [25,32]. When it is in the regime of transonic flow, the ratio of the jet velocity to the freestream velocity is decreased, so is the required C_μ. However, the previous studies are for regular CFJ airfoil with the suction slot very close to the TE. For CFJ control surfaces with the CFJ applied on the flap, the CFJ is expected to remain effective up to transonic flow, but future study needs to be done to confirm.

Figure 12 shows the streamlines of the baseline and CFJ control surfaces with C_μ of 0.025. It shows that the baseline control surface (left) has TE spanwise vortex formed starting from the root vortex connected to the tip vortex. With a small C_μ of 0.025, the TE spanwise vortex structure is removed due to no flow separation even though the streamlines are still swept toward the tip. The root and tip vortices become weaker. This benefits the control surface with the lift coefficient increased by 28% without increasing the total drag coefficient as indicated in Table 3. The low CFJ power coefficient due to the small C_μ increases the system overall corrected aerodynamic efficiency.

With the C_μ increased to 0.26 as shown in Fig. 13a, not just the TE spanwise vortex is removed, the streamlines are very well aligned with the freestream direction with little sweep toward to the tip. As expected, the lift coefficient is increased by 99% from 0.75 to 1.49 with the drag coefficient reduced by 54% from 0.108 to 0.05. The Mach contour in Fig. 13b also shows that the maximum injection Mach number reaches 0.74 (not the component normal to the injection slot), which increases the CFJ power coefficient substantially as shown in Table 3. The lift coefficient can be continuously increased, but the power coefficient will be also increased rapidly.

Figure 14 shows the comparison of the C_p distributions at the three span locations between the baseline and CFJ control surfaces. The higher the C_μ, the larger the area enclosed by the C_p line. The suction peak effect contributes to the lift enhancement at two locations, the LE due to the CFJ injection effect and the flap deflection location due to the CFJ jet suction effect. A phenomenon not observed in the regular CFJ wings without flaps is that the second pressure suction peak at the flap deflection location is significantly higher than the LE suction peak along the whole span for all the C_μ. This phenomenon also exists for the baseline control surface, but only at the inner span as shown in Fig. 7a. The LE suction peak is dominant at the midspan and outer span for the baseline control surface as shown in Figs. 7b and 7c. The phenomenon of the second suction peak being substantially higher for the CFJ appears to be attributed to two reasons: 1) the low pressure from the jet suction slot decreases the local pressure; 2) the attached flow experiences a rapid turning due to the flap deflection, which creates a local centrifugal acceleration that further reduces the pressure, as shown in Fig. 15.

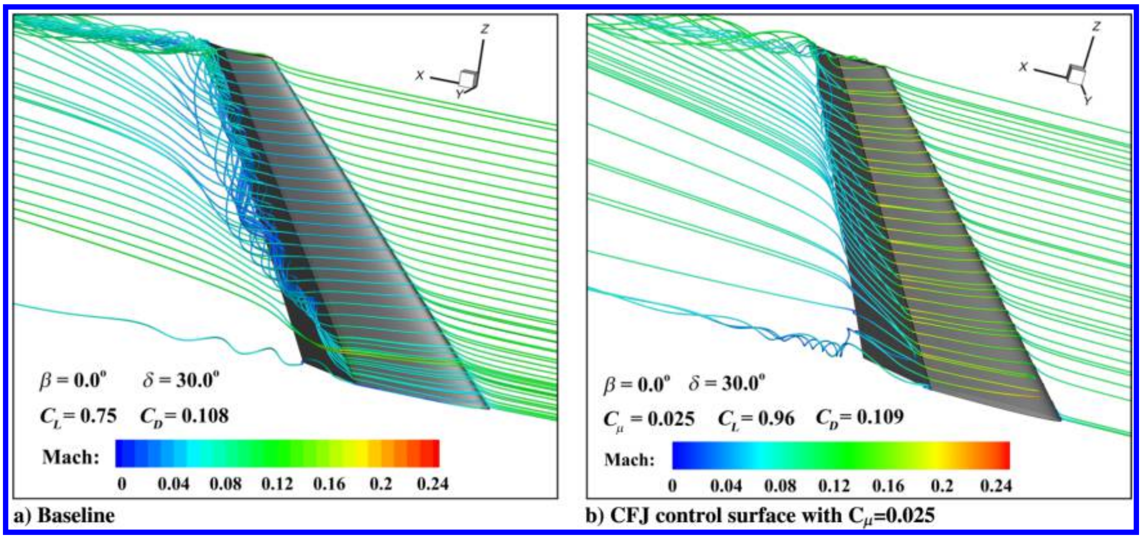

Fig. 12 Streamlines of the baseline and the CFJ control surfaces.

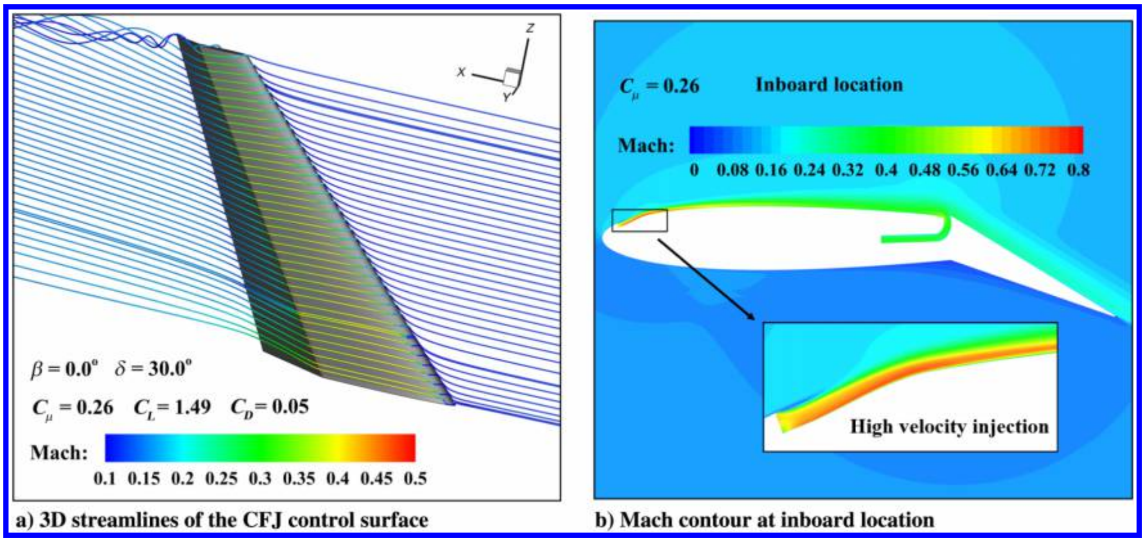

Fig. 13 Flow details of the CFJ control surface with $C_{\mu} = 0.26$.

B. Sideslip Angle β Variation

The baseline and CFJ control surface performance with varying sideslip angles β are studied in this section. The flap deflection angle δ is fixed at 30° and the simulated C_{μ} are 0.025, 0.05, and 0.26. Figure 9 plots lift coefficient C_L, aerodynamic efficiency C_L/C_D, corrected aerodynamic efficiency $(C_L/C_D)_c$, and power coefficient P_c versus sideslip angle β. As it is shown in Figs. 16a and 16b, the baseline control surface stalls at $\beta = 12.5°$, whereas the CFJ control surfaces achieve the stall angle of 17.5° at $C_{\mu} = 0.05$ and 27.5° at $C_{\mu} = 0.26$. With the flap deflection angle of 30°, the AoA of the CFJ control surface is 57.5° at β of 27.5°. Figure 16c shows that at low $C_{\mu} = 0.025$ and 0.05, $(C_L/C_D)_c$ decreases as β angle increases. However, at high $C_{\mu} = 0.26$, $(C_L/C_D)_c$ first increases to a peak value at $\beta = 12.5°$ and then decreases until stall. This pattern can be explained by the characteristics of P_c plots shown in Fig. 16d. In high C_{μ}, $(C_L/C_D)_c$ is dominated by the P_c term. The higher the P_c, the lower the $(C_L/C_D)_c$.

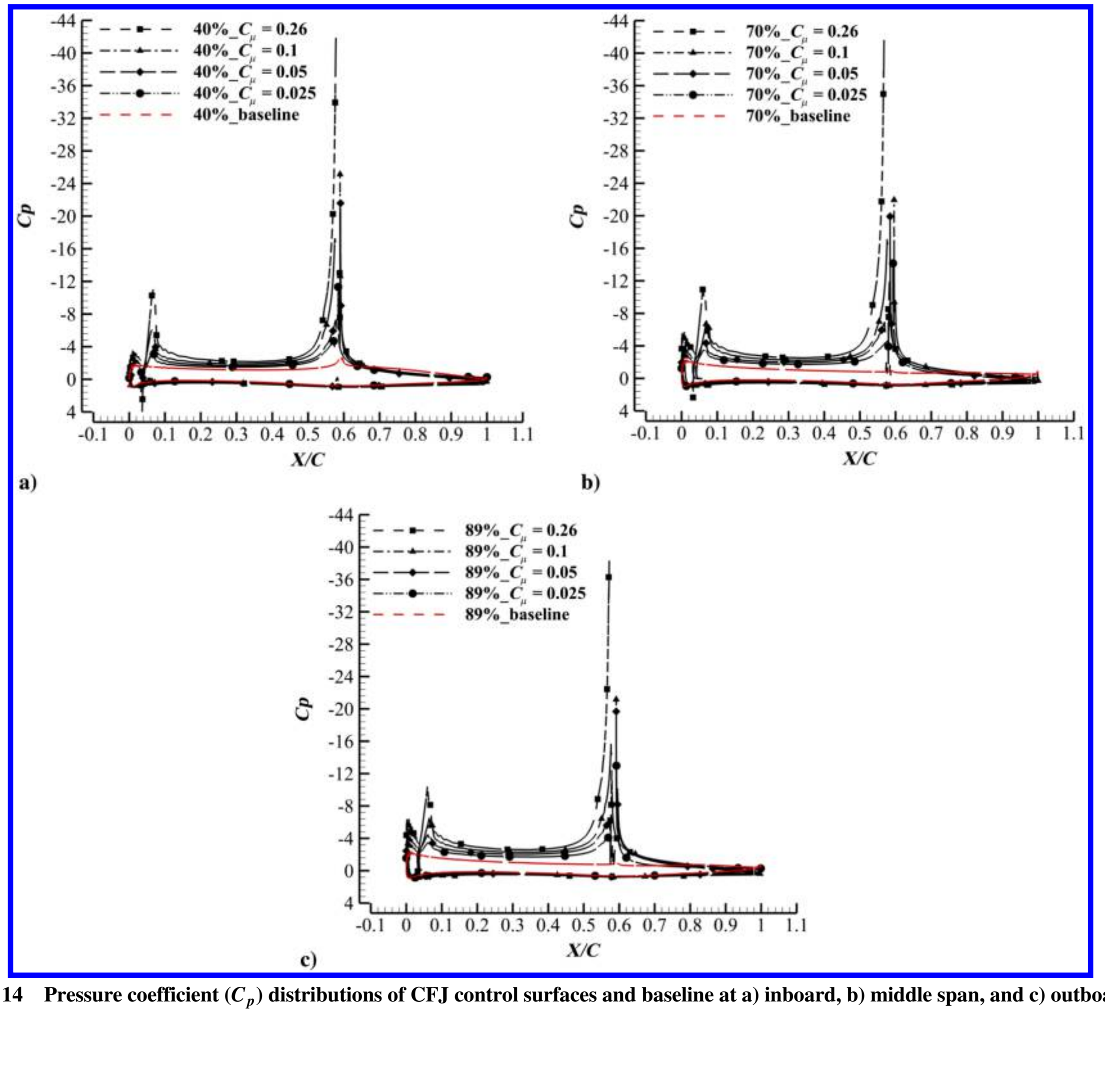

Fig. 14 Pressure coefficient (C_p) distributions of CFJ control surfaces and baseline at a) inboard, b) middle span, and c) outboard.

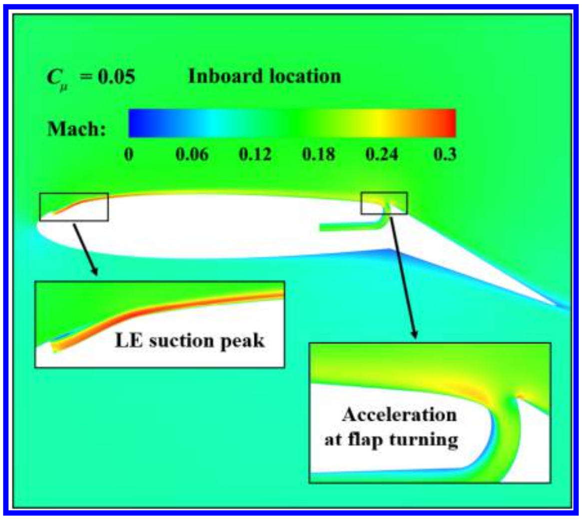

Fig. 15 Mach contour at inboard location with $C_\mu = 0.05$.

As β angle increases, LE suction peak is gradually enhanced, which decreases local static pressure and results in lower power consumption for CFJ injection. Once β angle passes 12.5°, the boundary layer is significantly deteriorated by the severe adverse pressure gradient and suffers a very large loss. The power required to pump the CFJ is thus increased at higher β angle. This is consistent with the experimental observation for the CFJ power variation with the AoA [5].

Figure 17 presents the streamlines of the CFJ control surface at a very high β of 27.5°. The flow is very well attached along major portion of the CFJ rudder flap, and minor flow separation is observed at the tip region due to the interaction of spanwise flow and tip vortex.

C. Flap Deflection Angle δ Variation

The CFJ control surfaces flap deflection angle at $\delta = 30°$, 40°, and 50° are studied in this section. The sideslip angle β is fixed at 0° and C_μ ranges from 0.025 to 0.26. Figures 18a–18c plot the C_L, C_L/C_D, and $(C_L/C_D)_c$ of the three deflection angles at various C_μ. At the same C_μ, the higher the deflection angle, the larger the increment of C_L. But this pattern is not held at low C_μ ranging from 0.025 to 0.1, because at high δ angle of 40° and 50°, a small C_μ is not sufficient to attach the flow. As shown in Figs. 19a and 19b, the flow is separated at C_μ of 0.025 and δ at 40° and 50°. At a high C_μ of 0.26, the flow is fully attached on the flap as shown in Figs. 19c and 19d, and a very high C_L of 1.88 and 2.12 is achieved at 0° sideslip angle with δ of 40° and 50°, respectively.

D. Discussion on Flow Control

For all AFC techniques, there are two figures of merit: 1) effectiveness and 2) efficiency. Effectiveness quantifies performance, specifically the lift augment, drag reduction, and stall AoA increase. Efficiency quantifies system benefit versus cost and involves two aspects: 1) power required by the AFC, and 2) power conversion efficiency of the AFC system. This efficiency determines how much

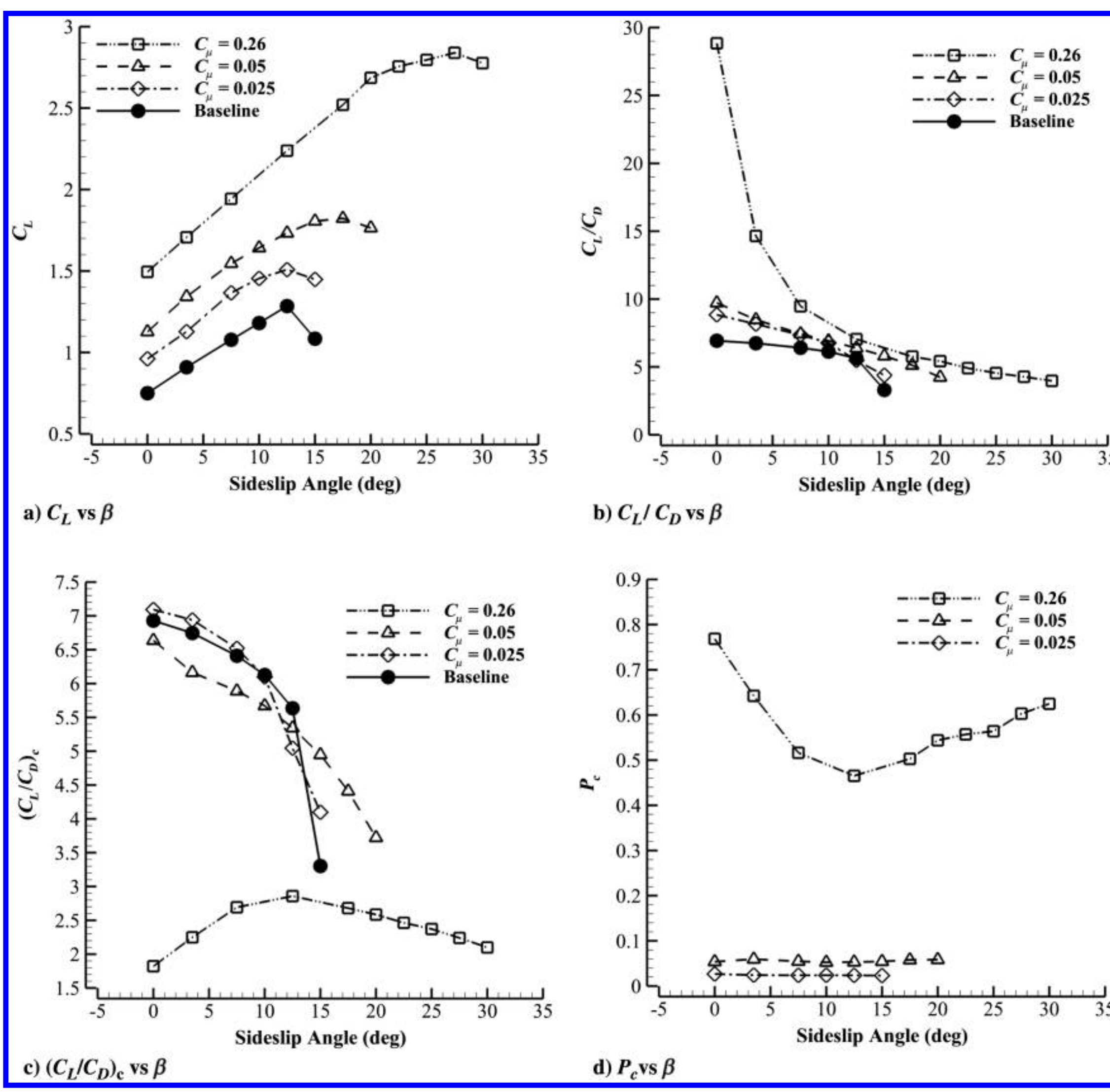

Fig. 16 Aerodynamic coefficients of CFJ control surfaces with various sideslip angles at deflection angle of 30°.

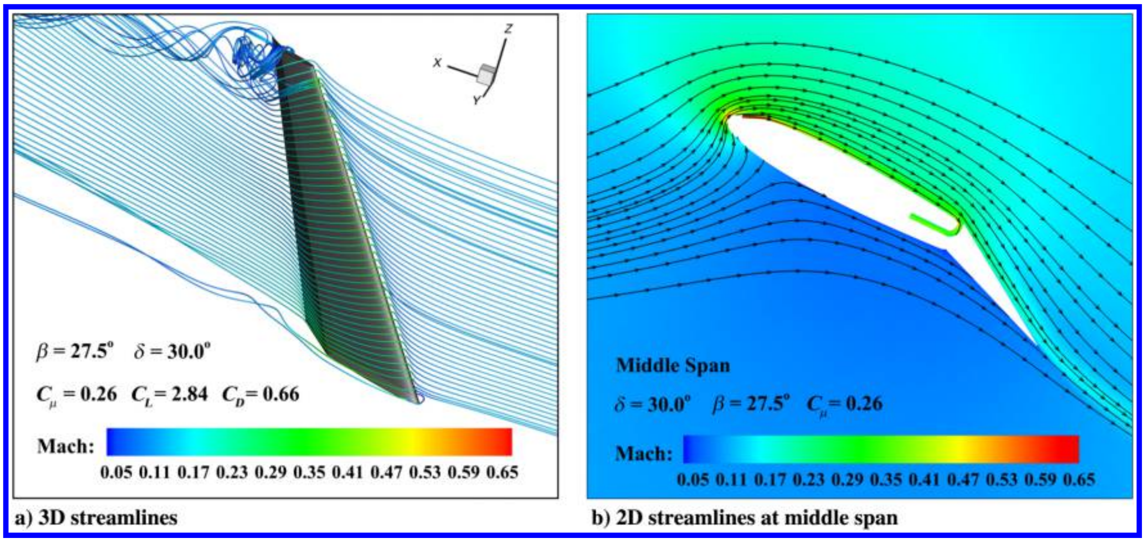

Fig. 17 Streamlines of the CFJ control surface at $\beta = 27.5°$, $C_\mu = 0.26$.

energy is transmitted to the controlled flow and is a key feature determining the overall performance of an AFC.

The widely studied sweeping jet (SWJ) based on the Coanda effect [59] has the advantage to significantly increase lift coefficient and is a well-studied flow control method that has been tested in various experiments. The disadvantages are as follows: 1) it requires an external fluid source (e.g., engine bleed) because it is not ZNMF, and it penalizes the system efficiency and even may not always be available; 2) the power and energy consumption are high. This is because SWJ in general requires high jet velocity to reduce mass flow, which suffers high energy loss. The massive flow separation and recirculation flow mechanism required by the SWJ exacerbate

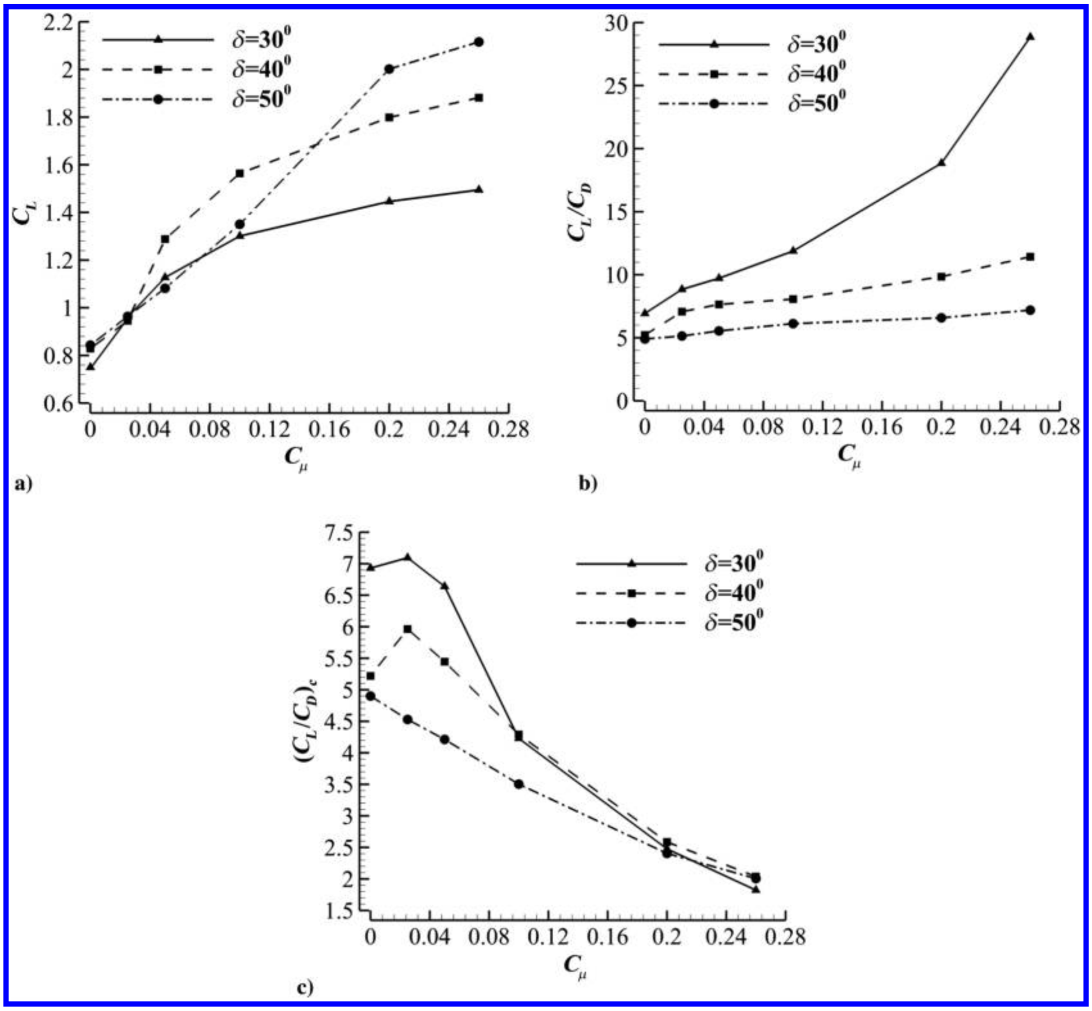

Fig. 18 CFJ control surface parameters vs CFJ momentum coefficient: a) lift coefficient; b) ratio of lift to drag; 3) corrected aerodynamic efficiency.

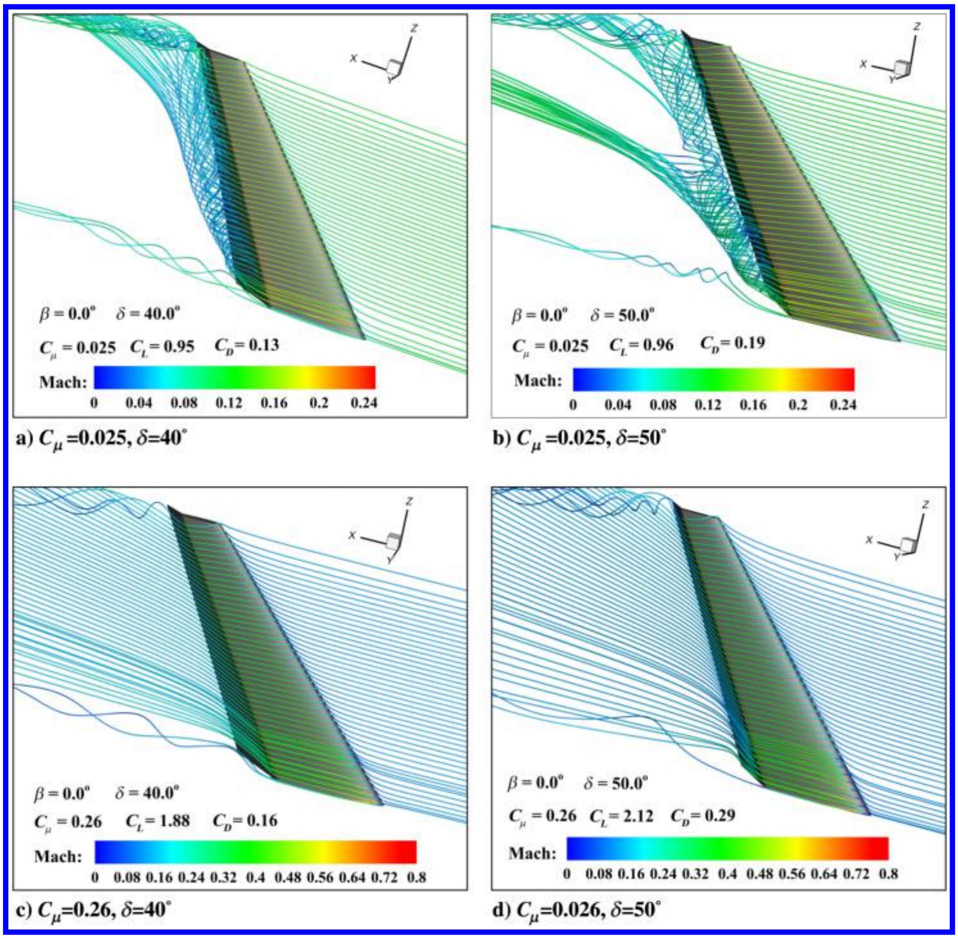

Fig. 19 Streamlines of the baseline and CFJ control surfaces.

the situation. The total pressure ratio required is thus very high. As indicated by Eq. (7), the power required for AFC is determined exponentially by the total pressure ratio.

The CFJ AFC is demonstrated to be an effective and efficient AFC, which dramatically enhances lift coefficient, reduces drag coefficient, and increases stall AoA at low energy expenditure with ZNMF. The CFJ actuator requires a small total pressure ratio Γ of no more than 1.2 as presented in Table 3, which significantly reduces the energy consumption. Additionally, the CFJ microcompressor actuators can achieve energy conversion efficiency at 80% or higher [27,30]. The disadvantage of CFJ is that it is a new flow control and is not mature yet. More research efforts need to be made to address some gaps, including CFJ microcompressor integration with the CFJ control surface, and the jet deflection with swept control surfaces.

VI. Conclusions

The numerical study in this paper suggests that the 3D CFJ control surfaces can achieve a very high control authority with ZNMF flow control at low energy expenditure. Numerical simulation is conducted with unsteady IDDES simulation due to the highly unsteady flow of the tip vortex, root vortex, and the massive flow separation at flap. The effects of CFJ momentum coefficient C_μ, sideslip angle β, and deflection angle δ are investigated. The validated results achieve a good agreement with experiment for the baseline control surface, which has the flap deflection angle of 30°. The maximum discrepancy between the predicted and measured coefficient of lift and drag is less than 3.8%. A small C_μ of 0.025 generates a 28% C_L increase at 0° sideslip angle with a higher corrected aerodynamic efficiency $(C_L/C_D)_c$ than the baseline case. At the C_μ of 0.26, the C_L is increased by 99.25% at 0° sideslip angle and the C_D drops by 52% due to removal of the flow separation at the flap and the suppression of the tip and root vortices by the CFJ. A phenomenon observed is that the second suction peak at the flap deflection point is higher than the LE suction peak. It is attributed to the low pressure of the CFJ suction and the attached flow experiencing a rapid turning due to the flap deflection, which creates a local radial acceleration that further reduces the pressure. CFJ control surface can also sustain a much higher stall sideslip angle than the baseline control surface. With C_μ of 0.26, CFJ control surface stalls at the sideslip angle of 27.5°, which is 2.2 times higher than the 12.5° for the baseline control surface, and a very high C_L of 2.84 is achieved. Furthermore, a CFJ control surface can tolerate very large flap deflection angle with the flow attached and a very high lift coefficient. At C_μ of 0.26 and 0° sideslip angle, very high C_L of 1.88 and 2.12, 2.3, and 2.5 times of the baseline cases are achieved at δ of 40° and 50°. The next-step study is to conduct wind tunnel testing to experimentally prove the CFJ control surface performance.

Acknowledgment

The authors would like to acknowledge the computing resource provided by the Center for Computational Sciences at the University of Miami. The authors would also like to express their gratitude to Veer Vatsa of NASA Langley research center and Damiano Casalino of TU Delft for the valuable discussion regarding the validation of baseline control surface simulation. The University of Miami and Dr. Gecheng Zha may receive royalties for future commercialization of the intellectual property used in this study.

References

[1] Anders, S., Sellers, W., III, and Washburn, A., “Active Flow Control Activities at NASA Langley,” *2nd AIAA Flow Control Conference*, AIAA Paper 2004-2623, June–July 2004. https://doi.org/10.2514/6.2004-2623

[2] Zha, G.-C., Carroll, B. F., Paxton, C. D., Conley, C. A., and Wells, A., "High-Performance Airfoil Using Coflow Jet Flow Control," *AIAA Journal*, Vol. 45, No. 8, 2007, pp. 2087–2090. https://doi.org/10.2514/1.20926

[3] Bower, W., and Kibens, V., "An Overview of Active Flow Control Applications at the Boeing Company," *2nd AIAA Flow Control Conference*, AIAA Paper 2004-2624, June–July 2004. https://doi.org/10.2514/6.2004-2624

[4] Kandil, O., Gercek, E., Zheng, X., and Luo, X., "Development of Computational Sensing and Active Flow Control of Airfoils During Dynamic Stall," *42nd AIAA Aerospace Sciences Meeting and Exhibit*, AIAA Paper 2004-0043, 2004. https://doi.org/10.2514/6.2004-43

[5] Lefebvre, A., Dano, B., Bartow, W., Fronzo, M., and Zha, G., "Performance and Energy Expenditure of Coflow Jet Airfoil with Variation of Mach Number," *Journal of Aircraft*, Vol. 53, No. 6, 2016, pp. 1757–1767. https://doi.org/10.2514/1.C033113

[6] Van Buren, T., and Amitay, M., "Comparison Between Finite-Span Steady and Synthetic Jets Issued into a Quiescent Fluid," *Experimental Thermal and Fluid Science*, Vol. 75, July 2016, pp. 16–24. https://doi.org/10.1016/j.expthermflusci.2016.01.014

[7] Pack, L., Schaeffler, N., Yao, C., and Seifert, A., "Active Control of Flow Separation from the Slat Shoulder of a Supercritical Airfoil," *1st Flow Control Conference*, AIAA Paper 2002-3156, June 2002. https://doi.org/10.2514/6.2002-3156

[8] Rathay, N. W., Boucher, M. J., Amitay, M., and Whalen, E., "Performance Enhancement of a Vertical Tail Using Synthetic Jet Actuators," *AIAA Journal*, Vol. 52, No. 4, 2014, pp. 810–820. https://doi.org/10.2514/1.J052645

[9] Lin, J. C., Andino, M. Y., Alexander, M. G., Whalen, E. A., Spoor, M. A., Tran, J. T., and Wygnanski, I. J., "An Overview of Active Flow Control Enhanced Vertical Tail Technology Development," *54th AIAA Aerospace Sciences Meeting*, AIAA Paper 2016-0056, Jan. 2016. https://doi.org/10.2514/6.2016-0056

[10] Andino, M. Y., Lin, J. C., Washburn, A. E., Whalen, E. A., Graff, E. C., and Wygnanski, I. J., "Flow Separation Control on a Full-Scale Vertical Tail Model Using Sweeping Jet Actuators," *53rd AIAA Aerospace Sciences Meeting*, AIAA Paper 2015-0785, Jan. 2015. https://doi.org/10.2514/6.2015-0785

[11] Seele, R., Graff, E., Gharib, M., Taubert, L., Lin, J., and Wygnanski, I., "Improving Rudder Effectiveness with Sweeping Jet Actuators," *6th AIAA Flow Control Conference*, AIAA Paper 2012-3244, June 2012. https://doi.org/10.2514/6.2012-3244

[12] Seele, R., Graff, E., Lin, J., and Wygnanski, I., "Performance Enhancement of a Vertical Tail Model with Sweeping Jet Actuators," *51st AIAA Aerospace Sciences Meeting Including the New Horizons Forum and Aerospace Exposition*, AIAA Paper 2013-0411, Jan. 2013. https://doi.org/10.2514/6.2013-411

[13] Rathay, N., Boucher, M., Amitay, M., and Whalen, E., "Parametric Study of Synthetic-Jet-Based Control for Performance Enhancement of a Vertical Tail," *AIAA Journal*, Vol. 52, No. 11, 2014, pp. 2440–2454. https://doi.org/10.2514/1.J052887

[14] Graff, E., Seele, R., Lin, J. C., and Wygnanski, I., "Sweeping Jet Actuators—A New Design Tool for High Lift Generation," *20130013994, Proceedings of Innovative Control Effectors for Military Vehicles Symposium*, Paper AVT-215, Stockholm, Sweden, May 2013.

[15] Shmilovich, A., Yadlin, Y., and Whalen, E., "Computational Evaluation of Flow Control for Enhanced Control Authority of a Vertical Tail," *AIAA Journal*, Vol. 54, No. 8, 2016, pp. 2211–2220. https://doi.org/10.2514/1.J054712

[16] Kara, K., "Numerical Simulation of a Sweeping Jet Actuator," *34th AIAA Applied Aerodynamics Conference*, AIAA Paper 2016-3261, June 2016. https://doi.org/10.2514/6.2016-3261

[17] Kara, K., "Numerical Study of Internal Flow Structures in a Sweeping Jet Actuator," *33rd AIAA Applied Aerodynamics Conference*, AIAA Paper 2015-2424, June 2015. https://doi.org/10.2514/6.2015-2424.

[18] Zhang, J., Xu, K., Yang, Y., Ren, Y., Patel, P., and Zha, G., "Aircraft Control Surfaces Using Co-Flow Jet Active Flow Control Airfoil," *2018 Applied Aerodynamics Conference*, AIAA Paper 2018-3067, June 2018. https://doi.org/10.2514/6.2018-3067

[19] Zha, G., Gao, W., and Paxton, C. D., "Jet Effects on Co-Flow Jet Airfoil Performance," *AIAA Journal*, Vol. 45, No. 6, 2007, pp. 1222–1231. https://doi.org/10.2514/1.23995

[20] Zha, G.-C., Paxton, C., Conley, A., Wells, A., and Carroll, B., "Effect of Injection Slot Size on High Performance Co-Flow Jet Airfoil," *Journal of Aircraft*, Vol. 43, No. 4, 2006, pp. 987–995. https://doi.org/10.2514/1.16999

[21] Wang, B., Haddoukessouni, B., Levy, J., and Zha, G.-C., "Numerical Investigations of Injection-Slot-Size Effect on the Performance of Coflow Jet Airfoils," *Journal of Aircraft*, Vol. 45, No. 6, 2008, pp. 2084–2091. https://doi.org/10.2514/1.37441

[22] Dano, B. P. E., Kirk, D., and Zha, G.-C., "Experimental Investigation of Jet Mixing Mechanism of Co-Flow Jet Airfoil," *5th AIAA Flow Control Conference*, AIAA Paper 2010-4421, July 2010. https://doi.org/10.2514/6.2010-4421

[23] Dano, B., Zha, G., and Castillo, M., "Experimental Study of Co-Flow Jet Airfoil Performance Enhancement Using Discreet Jets," *49th AIAA Aerospace Sciences Meeting Including the New Horizons Forum and Aerospace Exposition*, AIAA Paper 2011-941, Jan. 2011. https://doi.org/10.2514/6.2011-941

[24] Lefebvre, A., and Zha, G.-C., "Design of High Wing Loading Compact Electric Airplane Utilizing Co-Flow Jet Flow Control," *AIAA SciTech 2015: 53rd Aerospace Sciences Meeting*, AIAA Paper 2015-0772, Jan. 2015. https://doi.org/10.2514/6.2015-0772

[25] Liu, Z.-X., and Zha, G.-C., "Transonic Airfoil Performance Enhancement Using Co-Flow Jet Active Flow Control," *AIAA Aviation*, AIAA Paper 2016-3472, June 2016. https://doi.org/10.2514/6.2016-3472

[26] Lefebvre, A., and Zha, G.-C., "Trade Study of 3D Co-Flow Jet Wing for Cruise and Takeoff/Landing Performance," *AIAA SciTech 2016, AIAA Aerospace Science Meeting*, AIAA Paper 2016-0570, Jan. 2016. https://doi.org/10.2514/6.2016-0570

[27] Zha, G., Yang, Y., Ren, Y., and McBreen, B., "Super-Lift and Thrusting Airfoil of Coflow Jet Actuated by Micro-Compressors," *2018 Flow Control Conference*, AIAA Paper 2018-3061, 2018. https://doi.org/10.2514/6.2018-3061

[28] Xu, K., Zhang, J., and Zha, G., "Drag Minimization of Co-Flow Jet Control Surfaces at Cruise Conditions," *AIAA SciTech 2019 Forum*, AIAA Paper 2019-1848, Jan. 2019. https://doi.org/10.2514/6.2019-1848

[29] Xu, K., and Zha, G., "High Control Authority 3D Aircraft Control Surfaces Using Co-Flow Jet," *AIAA Aviation 2019 Forum*, AIAA Paper 2019-3168, June 2019. https://doi.org/10.2514/6.2019-3168

[30] Xu, K., and Zha, G., "Design of High Specific Speed Mixed Flow Micro-Compressor for Co-Flow Jet Actuators," *IGTI Turbo Expo 2019*, American Soc. of Mechanical Engineers Paper GT2019-90980, Fairfield, NJ, June 2019. https://doi.org/10.1115/GT2019-90980

[31] Wang, Y., and Zha, G., "Study of Super-Lift Coefficient of Co-Flow Jet Airfoil and its Power Consumption," *AIAA Aviation 2019 Forum*, AIAA Paper 2019-3652, 2019. https://doi.org/10.2514/6.2019-3652

[32] Wang, Y., and Zha, G., "Study of Mach Number Effect for 2D Co-Flow Jet Airfoil at Cruise Conditions," *AIAA Aviation 2019 Forum*, AIAA Paper 2019-3169, 2019. https://doi.org/10.2514/6.2019-3169

[33] Shur, M. L., Spalart, P. R., Strelets, M. K., and Travin, A. K., "A Hybrid RANS-LES Approach with Delayed-DES and Wall-Modelled LES Capabilities," *International Journal of Heat and Fluid Flow*, Vol. 29, No. 6, 2008, pp. 1638–1649. https://doi.org/10.1016/j.ijheatfluidflow.2008.07.001

[34] Yang, Y., and Zha, G., "Simulation of Airfoil Stall Flows Using IDDES with High Order Schemes," *46th AIAA Fluid Dynamics Conference*, AIAA Paper 2016-3185, June 2016. https://doi.org/10.2514/6.2016-3185

[35] Yang, Y., and Zha, G., "Improved Delayed Detached Eddy Simulation of Super-Lift Coefficient of Subsonic Co-Flow Jet Flow Control Airfoil," *2018 AIAA Aerospace Sciences Meeting*, AIAA Paper 2018-0314, Jan. 2018. https://doi.org/10.2514/6.2018-0314

[36] Wang, B., and Zha, G.-C., "Detached-Eddy Simulation of a Coflow Jet Airfoil at High Angle of Attack," *Journal of Aircraft*, Vol. 48, No. 5, 2011, pp. 1495–1502. https://doi.org/10.2514/1.C000282

[37] Shen, Y.-Q., Zha, G.-C., and Wang, B.-Y., "Improvement of Stability and Accuracy of Implicit WENO Scheme," *AIAA Journal*, Vol. 47, No. 2, 2009, pp. 331–344. https://doi.org/10.2514/1.37697

[38] Shen, Y.-Q., Zha, G.-C., and Chen, X.-Y., "High Order Conservative Differencing for Viscous Terms and the Application to Vortex-Induced Vibration Flows," *Journal of Computational Physics*, Vol. 228, No. 22, 2009, pp. 8283–8300. https://doi.org/10.1016/j.jcp.2009.08.004

[39] Shen, Y.-Q., and Zha, G.-C., "Improvement of the WENO Scheme Smoothness Estimator," *International Journal for Numerical Methods in Fluids*, Vol. 64, No. 6, 2009, pp. 653–675. https://doi.org/10.1002/fld.2186

[40] Zha, G.-C., and Bilgen, E., "Numerical Study of Three-Dimensional Flows Using Unfactored Upwind-Relaxation Sweeping Algorithm," *Journal of Computational Physics*, Vol. 125, No. 2, 1996, pp. 425–433. https://doi.org/10.1006/jcph.1996.0104

[41] Wang, B., Hu, Z., and Zha, G.-C., "General Subdomain Boundary Mapping Procedure for Structured Grid Implicit CFD Parallel Computation," *Journal of Aerospace Computing, Information, and Communication*, Vol. 5, No. 11, 2008, pp. 425–447. https://doi.org/10.2514/1.35498

[42] Gan, J., Shen, Y., and Zha, G., "Comparison of Drag Prediction Using RANS Models and DDES for the DLR-F6 Configuration Using High Order Schemes," *54th AIAA Aerospace Sciences Meeting*, AIAA Paper 2016-0553, 2016. https://doi.org/10.2514/6.2016-0553

[43] Yang, Y., and Zha, G., "Numerical Investigation of Performance Improvement of the Co-Flow Jet Electric Airplane," *AIAA Aviation Forum*, AIAA Paper 2018-4208, 2018. https://doi.org/10.2514/6.2018-4208

[44] Im, H., Chen, X., and Zha, G., "Simulation of 3D Multistage Axial Compressor Using a Fully Conservative Sliding Boundary Condition," *ASME 2011 International Mechanical Engineering Congress and Exposition*, American Soc. of Mechanical Engineers, Fairfield, NJ, 2011, pp. 1321–1330. https://doi.org/10.1115/IMECE2011-62049

[45] Espinal, D., Im, H.-S., and Zha, G.-C., "Full-Annulus Simulation of Nonsynchronous Blade Vibration Excitation of an Axial Compressor," *Journal of Turbomachinery*, Vol. 140, No. 3, 2018, Paper 031008. https://doi.org/10.1115/1.4038337

[46] Im, H., and Zha, G., "Investigation of Flow Instability Mechanism Causing Compressor Rotor-Blade Nonsynchronous Vibration," *AIAA Journal*, Vol. 52, No. 9, 2014, pp. 2019–2031. https://doi.org/10.2514/1.J052781

[47] Im, H.-S., and Zha, G.-C., "Simulation of Non-Synchronous Blade Vibration of an Axial Compressor Using a Fully Coupled Fluid/Structure Interaction," *ASME Turbo Expo 2012: Turbine Technical Conference and Exposition*, American Soc. of Mechanical Engineers Paper GT2012-68150, Fairfield, NJ, 2012, pp. 1395–1407. https://doi.org/10.1115/GT2012-68150

[48] Gan, J., Im, H.-S., Espinal, D., Lefebvre, A., and Zha, G.-C., "Investigation of a Compressor Rotor Non-Synchronous Vibration with and Without Fluid-Structure Interaction," *ASME Turbo Expo 2014: Turbine Technical Conference and Exposition*, American Soc. of Mechanical Engineers Paper GT2014-26478, Fairfield, NJ, 2014. https://doi.org/10.1115/GT2014-26478

[49] Chen, X.-Y., and Zha, G.-C., "Fully Coupled Fluid-Structural Interactions Using an Efficient High Resolution Upwind Scheme," *Journal of Fluids and Structures*, Vol. 20, No. 8, 2005, pp. 1105–1125. https://doi.org/10.1016/j.jfluidstructs.2005.02.011

[50] Chen, X., Zha, G.-C., and Yang, M.-T., "Numerical Simulation of 3-D Wing Flutter with Fully Coupled Fluid–Structural Interaction," *Computers & Fluids*, Vol. 36, No. 5, 2006, pp. 856–867. https://doi.org/10.1016/j.compfluid.2006.08.005

[51] Gan, J.-Y., Im, H.-S., Chen, X.-Y., Zha, G.-C., and Pasiliao, C. L., "Delayed Detached Eddy Simulation of Wing Flutter Boundary Using High Order Schemes," *Journal of Fluids and Structures*, Vol. 71, May 2017, pp. 199–216. https://doi.org/10.1016/j.jfluidstructs.2017.03.002

[52] Chen, X., Im, H., and Zha, G.-C., "Fully Coupled Fluid-Structural Interaction of a Transonic Rotor at Near-Stall Conditions Using Detached Eddy Simulation," *49th AIAA Aerospace Sciences Meeting Including the New Horizons Forum and Aerospace Exposition*, AIAA Paper 2011-228, 2011. https://doi.org/10.2514/6.2011-228

[53] Chen, X., and Zha, G., "Fully Coupled Fluid-Structural Interaction in a Hybrid Cartesian-Body Fitted Grid System," *40th Fluid Dynamics Conference and Exhibit*, AIAA Paper 2010-4611, 2010. https://doi.org/10.2514/6.2010-4611

[54] Chen, X., and Zha, G., "Detached Eddy Simulation of 3-D Wing Flutter with Fully Coupled Fluid-Structural Interaction," *48th AIAA Aerospace Sciences Meeting Including the New Horizons Forum and Aerospace Exposition*, AIAA Paper 2010-53, 2010. https://doi.org/10.2514/6.2010-53

[55] Yang, Y., and Zha, G., "Super-Lift Coefficient of Active Flow Control Airfoil: What Is the Limit?" *AIAA SciTech 2017, 55th AIAA Aerospace Science Meeting*, AIAA Paper 2017-1693, Jan. 2017. https://doi.org/10.2514/6.2017-1693

[56] Im, H.-S., Zha, G.-C., and Dano, B. P. E., "Large Eddy Simulation of Coflow Jet Airfoil at High Angle of Attack," *Journal of Fluid Engineering*, Vol. 136, No. 2, 2014, Paper 021101. https://doi.org/10.1115/1.4025649

[57] Im, H.-S., and Zha, G.-C., "Delayed Detached Eddy Simulation of Airfoil Stall Flows Using High-Order Schemes," *Journal of Fluids Engineering*, Vol. 136, No. 11, 2014, Paper 111104. https://doi.org/10.1115/1.4027813

[58] Vatsa, V. N., Casalino, D., Lin, J. C., and Appelbaum, J., "Numerical Simulation of a High-Lift Configuration with Embedded Fluidic Actuators," *32nd AIAA Applied Aerodynamics Conference*, AIAA Paper 2014-2142, June 2014. https://doi.org/10.2514/6.2014-2142

[59] Kind, R.-J., "A Proposed Method of Circulation Control," Ph.D. Thesis, Univ. of Cambridge, Cambridge, England, U.K., June 1969.